Separation Science and Technology
Publication details, including instructions for authors and subscription information:
http://www.informaworld.com/smpp/title~content=t713708471

ADSORPTION AND DESORPTION CHARACTERISTICS OF AIR ON ZEOLITE 5A, 10X, AND 13X FIXED BEDS

Jeong-Geun Jee[a]; Myung-Kyu Park[a]; Han-Kyu Yoo[b]; Kangtaek Lee[a]; Chang-Ha Lee[a]
[a] Department of Chemical Engineering, Yonsei University, Seoul, Korea [b] Department of Civil and Environmental Engineering, Hanyang University, Ahnsan, Korea

Online publication date: 23 October 2002

To cite this Article Jee, Jeong-Geun , Park, Myung-Kyu , Yoo, Han-Kyu , Lee, Kangtaek and Lee, Chang-Ha(2002) 'ADSORPTION AND DESORPTION CHARACTERISTICS OF AIR ON ZEOLITE 5A, 10X, AND 13X FIXED BEDS', Separation Science and Technology, 37: 15, 3465 — 3490
To link to this Article: DOI: 10.1081/SS-120014437
URL: http://dx.doi.org/10.1081/SS-120014437

MARCEL DEKKER, INC. • 270 MADISON AVENUE • NEW YORK, NY 10016

SEPARATION SCIENCE AND TECHNOLOGY
Vol. 37, No. 15, pp. 3465–3490, 2002

ADSORPTION AND DESORPTION CHARACTERISTICS OF AIR ON ZEOLITE 5A, 10X, AND 13X FIXED BEDS

Jeong-Geun Jee,[1] Myung-Kyu Park,[1] Han-Kyu Yoo,[2] Kangtaek Lee,[1] and Chang-Ha Lee[1,*]

[1]Department of Chemical Engineering, Yonsei University, 134 Shinchon-dong, Sudaemun-gu, Seoul 120-749, Korea
[2]Department of Civil and Environmental Engineering, Hanyang University, Ahnsan, Korea

ABSTRACT

Adsorption and desorption experiments for the binary mixture (N_2/O_2; 79:21 vol%) on zeolite 5A, 10X, and 13X beds were performed to study the dynamic characteristics of air separation adsorption processes. Because the breakthrough and desorption curves showed a tail by temperature variance in the beds, a nonisothermal dynamic model incorporating mass and energy balances was applied to the simulation of adsorption dynamics using the Langmuir–Freundlich model and the LDF approximation. The breakthrough and desorption results were compared among three different beds with respect to the breakthrough and desorption times,

*Corresponding author. Fax: +82-2-312-6401; E-mail: leech@yonsei.ac.kr

DOI: 10.1081/SS-120014437
0149-6395 (Print); 1520-5754 (Online)

www.dekker.com

MARCEL DEKKER, INC. • 270 MADISON AVENUE • NEW YORK, NY 10016

tailing effect, and temperature variation with the effects of pressure and flow rate. On the basis of the similar bed density, the order of breakthrough time and desorption time was zeolite 10X, 13X, and 5A beds. Also, the O_2 MTZ of the zeolite 10X bed was slightly sharper than those of the zeolite 5A and 13X beds due to more favorable N_2 isotherm of zeolite 10X. Furthermore, the breakthrough curve of the zeolite 13X bed showed a relatively long tail. In addition, the breakthrough curves of the zeolite 5A and 13X were similar to adiabatic behavior, whereas that of the zeolite 10X bed showed an isothermal behavior. The N_2 desorption experiments were performed by O_2 purge under the high pressure conditions. The desorption behaviors were very similar to the results of the breakthrough study, while the thermal effect on the desorption curve was negligible at the beds. The tails of the desorption curves were prominent with a change in the purge flow rate and desorption pressure. In all the beds, the feed and purge rates were more important factors for deciding the breakthrough and desorption times than the adsorption and desorption pressures in the experimental range.

Key Words: N_2/O_2 mixture; Zeolite 5A, 10X, and 13X; Breakthrough; Desorption; Thermal effect

INTRODUCTION

Oxygen recovery from air is a very attractive and important topic because oxygen is widely used in many chemical processes such as the biological treatment of wastewater, oxygen supply in the steel industries, paper and pulp industries, glass melting furnaces, and medical O_2 supply devices.[1]

Pressure swing adsorption (PSA) process for air separation is used widely because the installation costs are relatively low and it is easy to operate. Recently, the high purity oxygen (99 + %) PSA processes are studied by using a bed packed with zeolite and carbon molecular sieve.[2,3] Furthermore, the rapid pressure swing adsorption (RPSA) process was introduced to produce oxygen that had comparatively low purity but high productivity.[4] As another challenge, the vacuum swing adsorption (VSA) process was proposed to produce the oxygen that has both high purity and high productivity.[5,6]

Understanding the dynamic characteristics of the adsorption and desorption steps in an adsorption process is crucial to achieving high working capacity for a

given adsorbent, and achieving a high working capacity for the heavy component is crucial to achieving good process efficiency. Hence, the breakthrough time, the shape of breakthrough curve, the desorption characteristics, and the thermal effect are the main factors to develop the performances of PSA processes.[7] In many breakthrough studies, the pressure and feed flow rate were assumed to be constant. However, Malek and Farooq[8] proposed that the effect of flow variation becomes significant for sorbate concentration. Therefore, they introduced the concept of mean residence time to consider this flow variation. Also, Sircar and Kumar[9] studied the heat effect on the breakthrough system comparing adiabatic and isothermal systems with nonisothermal and nonadiabatic systems. Furthermore, they studied the effect of the heat transfer coefficient between column and surroundings on the system operation. Xiu[10] derived an analytical solution of breakthrough curves in a fixed bed packed with ACF (activated carbon fiber), and a parabolic profile approximation solution for linear adsorption systems. However, only a few studies of desorption dynamics have been published. Yang et al.[11] indicated that the heavy components like CO_2 could not be completely desorbed by purging with light product in the zeolite 5A bed. Also, it was shown that the variation of interstitial velocity at adsorption and desorption steps had a great effect on product purity and productivity.[12,13]

In spite of the importance of studying breakthrough and desorption dynamics, in many studies about air separation systems using adsorption technology, the adsorbent was selected by only the comparison of adsorption isotherms, especially adsorption selectivity. However, to select an optimum adsorbent appropriate to the specific processes, the bed dynamics of adsorption and desorption at each adsorbent also need to be considered.

In this study, the adsorption and desorption characteristics of the fixed beds packed with zeolite 5A, 10X, and 13X that are used in many commercial O_2 PSA processes were compared. The experimental and theoretical results of the adsorption and desorption time, breakthrough curvature and thermal effect play an important role in selecting an optimum adsorbent and the design of PSA or PVSA processes.

EXPERIMENTAL STUDIES

Zeolite 5A (Grace and Davison Co.), 10X (Baylith, WE-G 639), and 13X (Baylith, WE-G 652) were used as adsorbents. Prior to each experimental run, the adsorbent was regenerated at 613K over night.

The binary mixture (N_2/O_2; 79:21 vol%) and pure oxygen (99.9 + %) were used as feed gases for adsorption and purge gas for desorption, respectively. As an initial condition, the adsorption experiments were conducted at the bed saturated by O_2 with the same adsorption pressure and the desorption

experiments were carried out at the bed saturated by N_2 with the same desorption pressure. The operating pressure was in the range 3–6 atm and the feed and purge flow rates were in the range 2–6 LSTP/min. And the inlet and surrounding temperatures at all of the operating conditions were in the range 298–299K. The more detailed experimental conditions are shown in Table 1.

A schematic diagram of the breakthrough apparatus is shown in Fig. 1. The adsorption bed was made of stainless-steel pipe with a length of 100 cm, an ID of 2.2 cm, and a wall thickness of 1.75 mm. Three resistance temperature detectors

Table 1. Operating Conditions for Breakthrough and Desorption Experiments

Breakthrough and Desorption Experiments			
Adsorbent	Run No.	Adsorption and Desorption Pressure (atm)	Feed and Purge Flow Rate (LSTP/min)
Zeolite 5A	Run 1	3	2
	Run 2		4
	Run 3		6
	Run 4	4.5	2
	Run 5		4
	Run 6		6
	Run 7	6	2
	Run 8		4
	Run 9		6
Zeolite 10X	Run 10	3	2
	Run 11		4
	Run 12		6
	Run 13	4.5	2
	Run 14		4
	Run 15		6
	Run 16	6	2
	Run 17		4
	Run 18		6
Zeolite 13X	Run 19	3	2
	Run 20		4
	Run 21		6
	Run 22	4.5	2
	Run 23		4
	Run 24		6
	Run 25	6	2
	Run 26		4
	Run 27		6

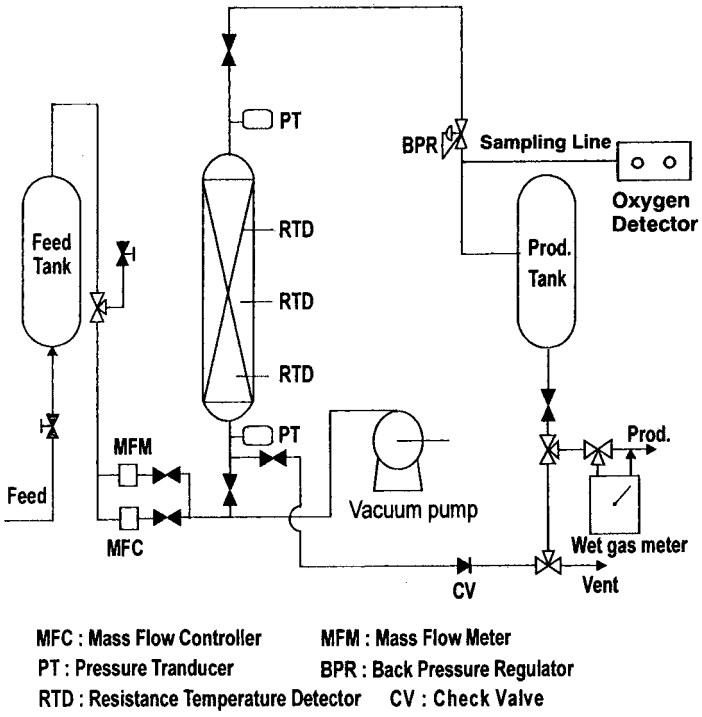

Figure 1. Schematic diagram of apparatus for breakthrough and desorption experiment.

(RTD, Pt 100 Ω) were installed at the positions of 10, 50, and 80 cm from the feed end to measure the temperature variations inside the bed. The flow rate was controlled by a mass-flow controller (Hastings, 2020-799 Hampton, Virginia, USA) and the total amount of feed and purge flow was measured by a wet gas meter (Sinagawa Co. W-NK-18, Japan). In order to keep the pressure in the adsorption bed constant, an electric back-pressure regulator was installed between the adsorption bed and the product bed. The experimental pressure was measured by two pressure transducers equipped at the top and bottom of the bed.

The concentration of the influent and effluent was analyzed by a portable oxygen analyzer (Teledyne Analytical Instruments, MDL 320B/RC-D, USA). This analyzer was confirmed by a mass spectrometer (Balzers, QME 200, Germany). The system was fully automated by a personal computer with a developed control program, and all measurements including flow rate, pressure, temperature, and O_2 concentration were saved on the computer through an AD converter (AXIOM Tech, AX540, Taiwan). The characteristics of adsorbents and adsorption beds are listed in Table 2.

Table 2. Characteristics of Adsorbents and Adsorption Bed

Properties	Adsorbents		
	Zeolite 5A	Zeolite 10X	Zeolite 13X
Type	Sphere	Sphere	Sphere
Average pellet radius, R_p (cm)	0.157	0.115	0.1
Bed density, ρ_B (g/cm^3)	0.795	0.820	0.78
Pellet density, ρ_p (g/cm^3)	1.16	1.1	1.05
Heat capacity, C_{ps} (cal/g K)[a]	0.22	0.27	0.32
Bed porosity, ε (–)	0.314	0.255	0.257
	Adsorption Bed		
Length, L (cm)	100		
Inside radius, R_{Bi} (cm)	1.1		
Outside radius, R_{Bo} (cm)	1.275		
Heat capacity of column, C_{pw} (cal/g K)	0.12		
Density of column, ρ_w (g/cm^3)	7.83		
Internal heat transfer coefficient, h_i (cal/cm^2 K sec)[b]	9.2×10^{-4}		
External heat transfer coefficient, h_o (cal/cm^2 K sec)	3.4×10^{-4}		

[a] These values were obtained from Refs. [5,21,28].
[b] These values were obtained from Ref. [21].

MATHEMATICAL MODEL

To understand the dynamic behaviors of the fixed bed during adsorption and desorption experiments, the mathematical models were developed on the basis of the following typical assumptions: (i) the gas phase behaves as an ideal gas mixture, (ii) radial concentration and temperature gradients are negligible, (iii) thermal equilibrium between adsorbents and bulk flow is assumed, (iv) the flow pattern is described by the axially dispersed plug flow model, (v) the mass transfer rate is represented by an LDF model, and (vi) the pressure drop along the bed is neglected.[14–17]

The breakthrough times in adsorption and desorption are different depending on the adsorption capacity of each adsorbent, the adsorbent amount packed in the bed, and other operating variables such as adsorption pressure, feed flow rate, etc. For that reason, to compare the adsorption and desorption characteristics of all adsorbents at the same operating conditions, dimensionless parameters need to be introduced such as dimensionless time τ, dimensionless

temperature Θ, and mole fraction of each component y_i. Therefore, the governing equations with the initial and boundary conditions from the previous works[18–20] were transformed by the following equations.

The dimensionless parameters used in simulation were defined as follows:

Dimensionless parameters

$$\tau = \frac{t}{t_0}, \quad x = \frac{z}{L}, \quad y = \frac{c}{c_0}, \quad U = \frac{u}{u_0}, \quad \bar{Q} = \frac{\bar{q}}{q_0}, \quad Q^* = \frac{q^*}{q_0}$$

$$\hat{B}_i = p_0 B_i, \quad \hat{\omega}_i = t_o \omega_i, Q_{\mathrm{m}_i} = \frac{q_{\mathrm{m}_i}}{q_{\mathrm{o}}}, \quad \Theta = \frac{T}{T_{\mathrm{f}}}, \quad \Theta_{\mathrm{w}} = \frac{T_{\mathrm{w}}}{T_{\mathrm{f}}}$$

$$\Theta_{\mathrm{atm}} = \frac{T_{\mathrm{atm}}}{T_{\mathrm{f}}}, \quad P = \frac{p}{p_0}, \quad Pe = \frac{u_0 L}{D_{\mathrm{L}}}, \quad Pe_{\mathrm{T}} = \frac{\varepsilon u_0 L \rho_{\mathrm{g}} C_{\mathrm{pg}}}{K_{\mathrm{L}}} \tag{1}$$

Reference parameters

$$t_0 = \frac{L}{u_{\mathrm{o}}}, \quad q_0 = \frac{c_0}{\rho_{\mathrm{p}}}\left(\frac{\varepsilon}{1-\varepsilon}\right), \quad c_0 = \frac{p_0}{R_{\mathrm{g}} T_0} \tag{2}$$

The i component mass balance for the bulk phase in the adsorption column is given by

$$-\frac{1}{Pe}\frac{\partial^2 y_i}{\partial x^2} + \frac{\partial y_i}{\partial \tau} + U\frac{\partial y_i}{\partial x} + \frac{\partial \bar{Q}_i}{\partial \tau} = 0 \tag{3}$$

and the overall mass balance can be written as

$$-\frac{1}{Pe}\frac{\partial^2 y}{\partial x^2} + \frac{\partial y}{\partial \tau} + U\frac{\partial y}{\partial x} + \sum_{i=1}\frac{\partial \bar{Q}_i}{\partial \tau} = 0 \tag{4}$$

Another characteristic of the adsorption process is the temperature variation caused by the heats of adsorption and desorption. The extent of the temperature variation has a meaningful effect on the total process performance. For that reason, dimensionless energy balance for the gas phase is introduced as follows:

$$-\frac{1}{Pe_{\mathrm{T}}}\frac{\partial^2 \Theta}{\partial x^2} + \frac{\beta}{\varepsilon \rho_{\mathrm{p}} C_{\mathrm{pg}}}\frac{\partial \Theta}{\partial \tau} + U\frac{\partial \Theta}{\partial x} - \frac{(-\Delta H_i)c_0}{T_0 \rho_{\mathrm{g}} C_{\mathrm{pg}}}\sum_{i}^{n}\frac{\partial \bar{Q}_i}{\partial \tau} + \frac{2h_i L}{\varepsilon \rho_{\mathrm{p}} C_{\mathrm{pg}} R_{Bi} u_0}(\Theta - \Theta_{\mathrm{w}}) = 0 \tag{5}$$

where $\beta = \varepsilon_t \rho_g c_{Pg} + \rho_B c_{Ps}$, ε_t is the total void fraction ($= \varepsilon + (1 - \varepsilon)\varepsilon_p$), ρ_B is the bed density ($= (1 - \varepsilon)\rho_p$), and h_i is the internal heat transfer coefficient.

To consider the heat loss through a wall and the heat accumulation in the wall, another dimensionless energy balance for the wall of the adsorption bed was used.

$$\frac{\partial \Theta_w}{\partial \tau} - \frac{2\pi R_{Bi} h_i}{\rho_w c_{Pw} A_w} \frac{L}{u_0} (\Theta - \Theta_w) + \frac{2\pi R_{Bo} h_0}{\rho_w c_{Pw} A_w} \frac{L}{u_0} (\Theta_w - \Theta_{atm}) = 0 \tag{6}$$

where $A_w = \pi(R_{Bo}^2 - R_{Bi}^2)$.

The boundary and initial conditions of mass and energy balances are presented below. The well-known Danckwarts boundary conditions were applied.[21]

Boundary condition for fluid flow

$$-\frac{1}{Pe}\frac{\partial y_i}{\partial x}\bigg|_{x=0} = U(y_i|_{x=0^-} - y_i|_{x=0^+}); \frac{\partial y_i}{\partial x}\bigg|_{x=1} = 0 \tag{7}$$

Boundary condition for heat flow

$$-\frac{1}{Pe_T}\frac{\partial \Theta}{\partial x}\bigg|_{x=0} = \frac{U}{\varepsilon}(\Theta|_{z=0^-} - \Theta|_{z=0}); \frac{\partial \Theta}{\partial x}\bigg|_{x=1} = 0 \tag{8}$$

Velocity boundary condition

$$U|_{x=0} = 1; \frac{\partial U}{\partial x}\bigg|_{x=1} = 0 \tag{9}$$

Initial condition for fluid flow

$$\text{Clean bed} \quad y_i(x,0) = 0; \quad \bar{Q}_i(x,0) = 0 \tag{10-1}$$

$$\text{Saturated bed} \quad y_i(x,0) = y_0; \quad \bar{Q}_i(x,0) = Q_i^* \tag{10-2}$$

Initial condition for heat flow

$$\Theta(x,0) = \Theta_{atm} \tag{11}$$

In this study, Eq. (10-2) was used as an initial condition because the bed was saturated with pure oxygen or nitrogen (99.9 + %) before each run.

Sircar and Hufton[22] pointed out that the LDF model for gas adsorption kinetics is frequently and successfully used for the analysis of adsorption column dynamic data and for adsorptive process designs because of its simplicity, reasonable accuracy, and physical consistency. Also, because the

values of the diffusion time constants of O_2 are about 3–4 times greater than those of N_2 in all the adsorbents used in this study, kinetic selectivity is not prominent in this system.[23] For that reason, the sorption rate into an adsorbent pellet is described by the LDF model with a single lumped mass transfer parameter.

$$\frac{\partial \bar{Q}}{\partial \tau} = \hat{\omega}_i(Q_i - \bar{Q}_i), \quad \text{where } \hat{\omega} = \frac{kD_{ei}}{R_P^2}\frac{L}{u_0} \tag{12}$$

The multi-component adsorption equilibrium was predicted by following the extended Langmuir–Freundlich model (LRC model):

$$Q_i^* = \frac{Q_{m_i}\hat{B}_i(y_i\Theta)^{n_i}p_0^{n_i-1}}{1+\sum_{j=1}^{n}\hat{B}_j(y_j\Theta)^{n_j}p_0^{n_j-1}} \tag{13}$$

where $Q_{m_i} = k_1 + k_2T_f\Theta$, $\hat{B}_i = k_3p_0\exp(k_4/(T_f\Theta))$, and $n_i = k_5 + k_6/(T_f\Theta)$.

Figure 2 shows the adsorption isotherms of all the adsorbents measured by a volumetric method up to 10 atm. The adsorbed amounts of N_2 and O_2 on the adsorbents in this study were similar to the published equilibrium data.[24–27] The experimental adsorption equilibrium data measured at three different temperature conditions were fitted by the extended LRC model, Eq. (13), and the parameters are listed in Table 3. In Fig. 2(a), the N_2 isotherm of zeolite 10X showed very favorable shape and the crossover of the N_2 adsorption amounts between zeolite 10X and 13X occurred near 1.5 atm. In Fig. 2(b), the isotherms of O_2 on all

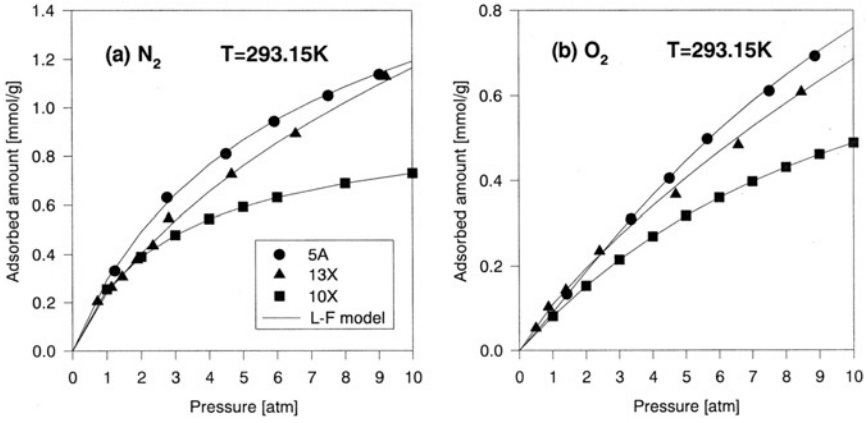

Figure 2. Equilibrium isotherms of (a) N_2 and (b) O_2 on the zeolite 5A, 10X, and 13X at 293.15K.

Table 3. LRC Parameters and LDF Coefficients for Zeolite 5A, 10X, and 13X

Adsorbent	Adsorbate	$k_1 \times 10^3$ (mol/g)	$k_2 \times 10^6$ (mol/g K)	$k_3 \times 10^6$ (1/atm)	k_4 (K)	k_5 (–)	k_6 (K)	LDF Coefficient, ω_i
5A	N_2	6.210	− 12.70	198.6	1970	2.266	− 396.5	0.05
	O_2	7.151	− 18.20	5419	662.6	− 1.101	656.4	0.15
10X	N_2	2.330	− 4.400	1.674	3586	1.384	− 142.1	0.046
	O_2	32.81	− 107.10	9866	578.9	3.552	− 797.4	0.13
13X	N_2	5.521	− 10.60	476.3	1683	1.107	− 30.74	0.032
	O_2	16.73	− 44.85	438.1	1108	1.984	− 307.5	0.12

adsorbents showed nearly linear shape. Also, the crossover of the O_2 adsorption amount between zeolite 5A and 13X was shown near 2.5 atm. As a result, the high adsorption pressure over 6–7 atm will decrease the adsorption selectivity between N_2 and O_2 because the N_2 isotherm is favorable, but the O_2 isotherm is linear in all the adsorbents.

The LDF coefficients of N_2 and O_2 on each zeolite were obtained by applying the LDF model, Eq. (12), to the breakthrough curve. At that time, the results measured by the uptake experiments in the previous work[28] were used as initial values. These LDF parameters were the same as the order of magnitude in the published papers[4,5,29] and these parameters for model simulation are listed in Table 3.

RESULTS AND DISCUSSION

Adsorption Characteristics

Effects of the Feed Flow Rate and Adsorption Pressure on the Adsorption Phenomena

The effects of the feed flow rate on the breakthrough curves for the three different adsorption beds are shown in Fig. 3. In all the beds, the linear increase of feed flow rate did not cause the linear decrease of breakthrough time because adsorbent loading is limited by mass transfer in the pellet at the larger feed flow rates. For that reason, the differences of breakthrough time between 2 and 4 LSTP/min were about 3–4 times larger than those between 4 and 6 LSTP/min at all the beds. On the basis of approximately the similar bed density in three different beds in Table 2, the order of breakthrough time was zeolite 10X, 13X, and 5A in Fig. 3.

The change of the breakthrough time in the zeolite 5A bed was compared with respect to the effects of adsorption pressure and feed flow rate in Fig. 4. In this figure, the breakthrough time was defined as the elapsed time decreased from 100 to 99% in the O_2 mole fraction. In Fig. 4(a), the breakthrough time decreased not linearly, but exponentially, with an increase in the feed flow rate. Therefore, the elongation of breakthrough time with an increase in adsorption pressure was larger at low feed flow rate in the range 1–3 LSTP/min than at high feed flow rate in the range 6–8 LSTP/min. In addition, the effect of the feed flow rate on the breakthrough time increased with an increase in the adsorption pressure. This is because the difference of adsorption amount between high and low adsorption pressures in Fig. 2 was reflected in the breakthrough time at low feed flow rate conditions, but not at high feed flow rate conditions.

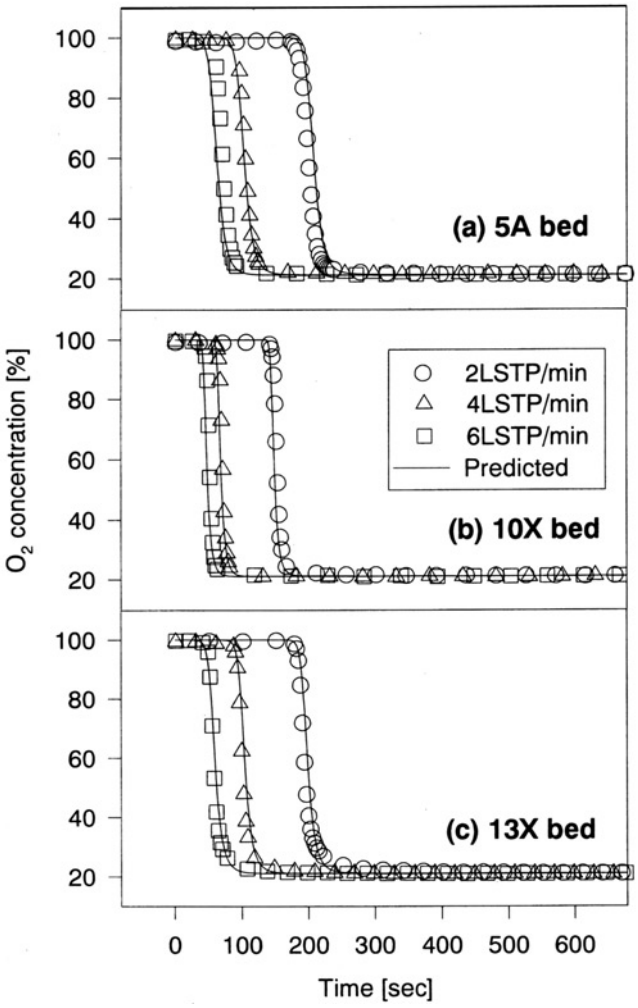

Figure 3. Experimental and predicted breakthrough curves of the zeolite (a) 5A, (b) 10X, and (c) 13X beds at 4.5 atm adsorption pressure.

In Fig. 4(b), the breakthrough time increased almost linearly with an increment in adsorption pressure. Moreover, the elongation of breakthrough time with adsorption pressure at the low feed rate condition was relatively steeper than that at the high feed rate condition. Comparing Fig. 4(a) and (b), the feed rate was a more important factor for deciding the breakthrough time than the adsorption pressure in the experimental range.

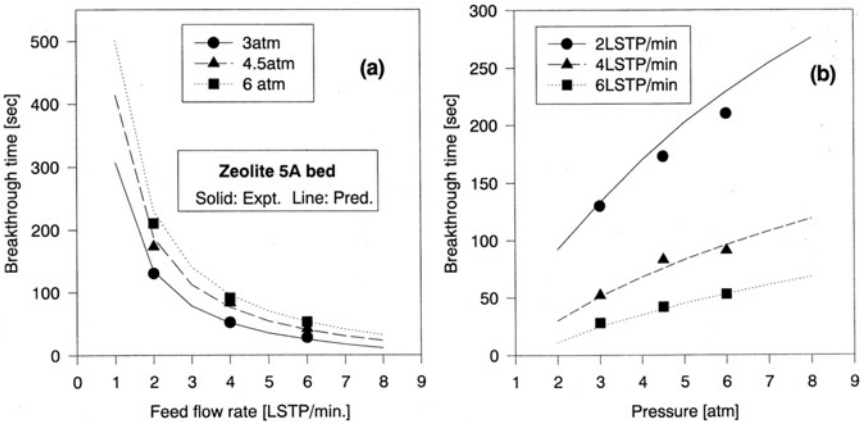

Figure 4. Effect of (a) feed flow rate and (b) adsorption pressure on the breakthrough time of the zeolite 5A bed.

Comparison of Adsorption Dynamics in Three Different Beds

Figure 5 shows a comparison of the breakthrough curves in three different adsorption beds in dimensionless form. In this study, the dimensionless time, τ, defined in Eqs. (1) and (2) was proportional to an interstitial velocity. Since the zeolite 5A bed had larger bed porosity than other beds, the interstitial velocity, that is, the dimensionless time at the zeolite 5A bed was smaller than those at other beds at the same feed rate condition. Therefore, in Fig. 7(a), the order of dimensionless breakthrough time was zeolite 10X, 5A, and 13X beds. With respect to the adsorption characteristics, the breakthrough curves of each adsorption bed showed more or less different behaviors. In the case of the zeolite 10X bed, the shape of the breakthrough curves was the steepest of all because the adsorption isotherm of N_2 on the zeolite 10X was relatively more favorable than others as shown in Fig. 2. Since the zeolite 13X bed showed a relatively long tail and broad shape of mass transfer zone (MTZ), this would have a bad effect on the working capacity of a given adsorbent bed even with long breakthrough time because of the increase of the unused bed area at adsorption step. The breakthrough curve in the zeolite 5A bed showed slightly shorter tailing and steeper breakthrough curve than those in the zeolite 13X bed.

Figure 6 shows the dimensionless temperature variation curves in the beds packed with each adsorbent. While the zeolite 5A bed showed the highest temperature peak among the three beds, the temperature decrease rate was the fastest. It was because the relatively low heat capacity of the pellet and high bed porosity of zeolite 5A in Table 2 caused the rapid change of temperature in the

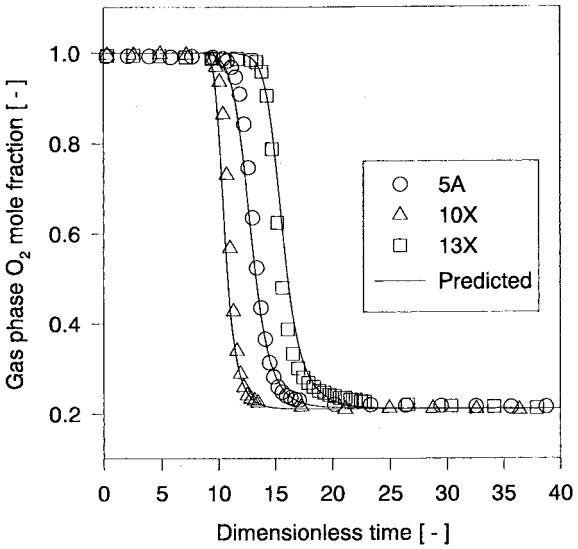

Figure 5. Comparisons of breakthrough curves among three different beds at 4.5 atm and 4 LSTP/min.

gas phase. Also, the broad temperature profile in the zeolite 13X bed caused a longer tail of concentration breakthrough curve than that in the zeolite 5A bed. In the case of the zeolite 10X bed, the tailing of temperature curve was similar to that in the zeolite 13X bed. However, the lowest temperature increase near to the isothermal condition in the zeolite 10X bed gave rise to the shortest tail of breakthrough curve shown in Fig. 5.

Figure 7 confirms the heat effect on the breakthrough curves by comparing among the isothermal, adiabatic, and nonisothermal/nonadiabatic conditions. Due to the long tail of temperature profiles in Fig. 6, the predicted breakthrough curves at nonisothermal/nonadiabatic conditions in all the beds were nearly the same as those at adiabatic condition. Especially, the differences of the breakthrough time between nonisothermal/nonadiabatic conditions and isothermal conditions were prominent in the zeolite 5A and 13X beds as shown in Fig. 7(a) and (c). However, in the zeolite 10X bed in Fig. 7(b), as mentioned previously, because of its isothermal tendency, the difference among breakthrough curves at each thermal condition was also nearly the same. In all the beds, the shape of the breakthrough curve in the experimental range was not changed by the thermal effect because of the small temperature excursion in Fig. 6. As a result, the adsorption heat effect on the adsorption behavior was not negligible, but small except in the zeolite 10X bed.

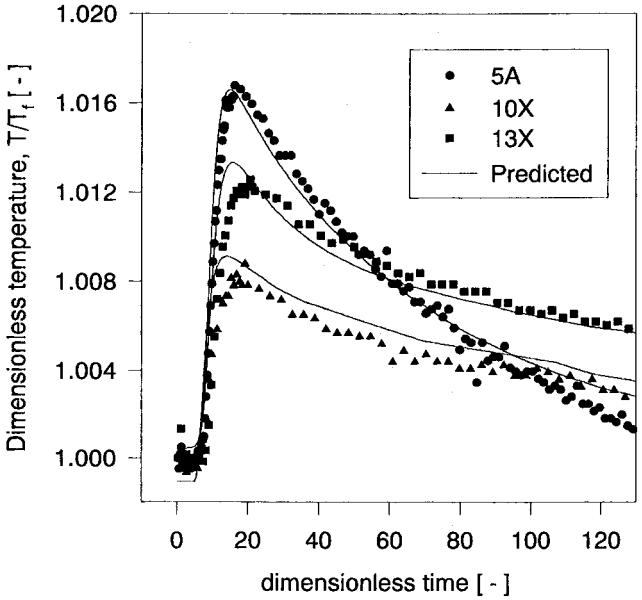

Figure 6. Experimental and predicted temperature curves of the breakthrough experiments in the middle of three different beds at 4.5 atm and 4 LSTP/min.

Desorption Characteristics

Effect of Purge Flow Rate and Desorption Pressure on the Desorption Phenomena

In this study, high pressure purge over ambient pressure was conducted to compare the desorption characteristics of three different adsorbent beds.[30] The desorption experiments were conducted by oxygen purge in the range 3–6 atm desorption pressure. As an initial condition, the bed was saturated by N_2 at the same experimental pressure. Also, desorption time is defined as the elapsed time that reaches the 99 + % O_2 mole fraction in effluent.

Figure 8 shows the effects of purge flow rate on the desorption curves in the three different adsorption beds. As shown in this figure, desorption time was elongated by the decrease of purge flow rate. Similar to the result of the adsorption behavior, the linear increase in purge rate did not lead to the linear decrease of desorption time in all the beds because the desorption of N_2 and the adsorption of O_2 are limited by mass transfer in the pellet at larger purge rates. However, unlike the results of breakthrough experiments, the smaller the purge

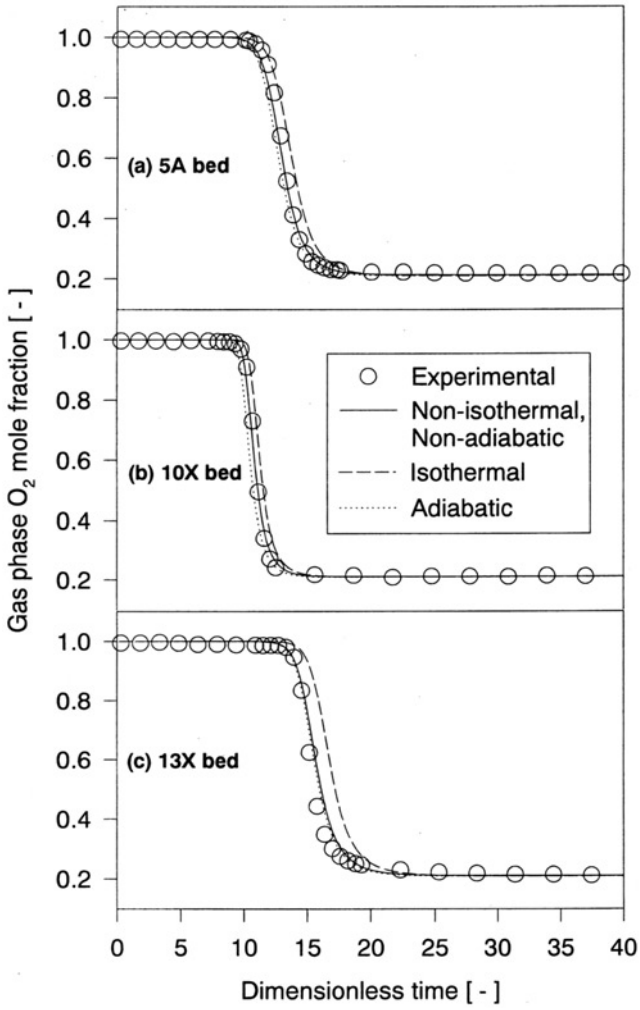

Figure 7. Comparisons of experimental and predicted breakthrough curves of the zeolite (a) 5A, (b) 10X, and (c) 13X beds on the three different temperature conditions at 4.5 atm and 4 LSTP/min.

flow rate and the higher the desorption pressure, the longer the tailing and the broader the desorption curve. Also, the order of desorption time was zeolite 10X, 13X, and 5A beds at the same purge condition.

The change of the desorption time in the zeolite 5A bed was compared in respect to the effects of desorption pressure and purge flow rate in Fig. 9. As

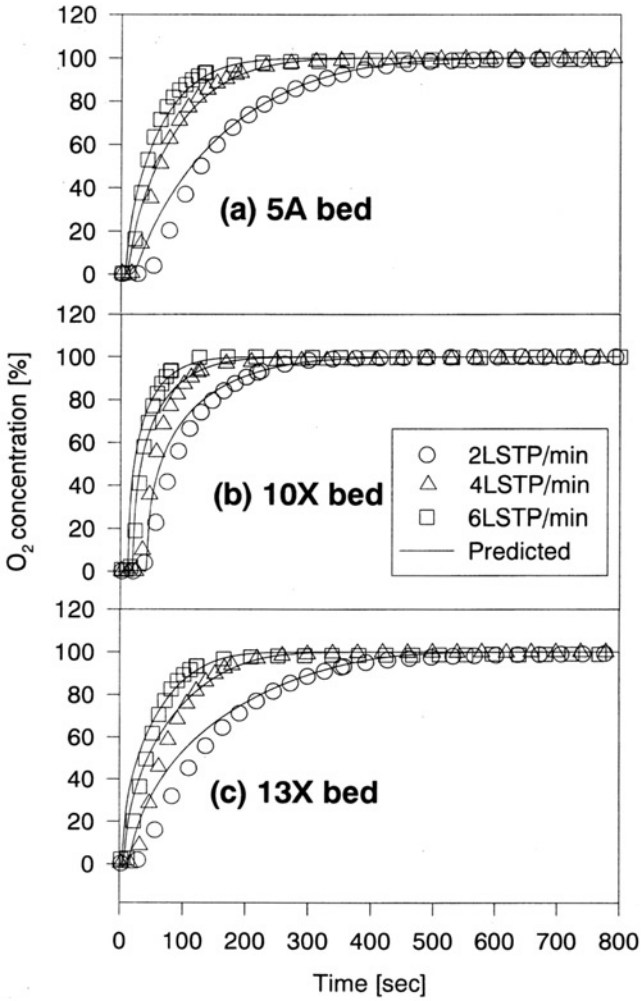

Figure 8. Experimental and predicted desorption curves of the zeolite (a) 5A, (b) 10X, and (c) 13X beds at 4.5 atm desorption pressure.

shown in Fig. 9(a), the desorption time drastically decreased with an increase in the purge flow rate in the range 1–3 LSTP/min. However, the advantage of increased purge rate disappeared over 6 LSTP/min. This suggests that the improvement in the regeneration rate by an increase in purge flow rate is limited by a certain purge flow rate. Figure 9(b) clearly shows that the effect of

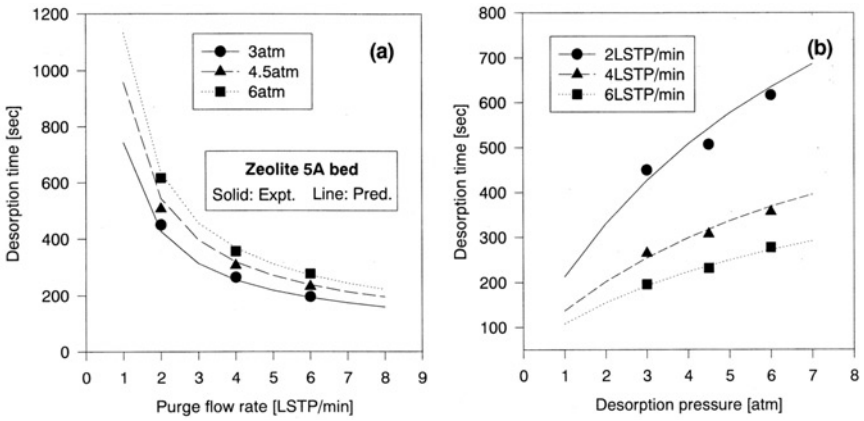

Figure 9. Effect of (a) purge flow rate and (b) desorption pressure on the desorption time of the zeolite 5A bed.

desorption pressure on desorption time in the low purge rates was more prominent than that in the high purge rates. However, the effect of purge flow rate on desorption time at the same desorption pressure condition was more significant than that of desorption pressure at the same purge flow rate in Fig. 9(a). Furthermore, this effect became more important with an increase in the desorption pressure. This implies that the purge rate plays a key role in determining the regeneration time in the highly adsorbed bed. In addition, in 4–6 LSTP/min purge flow rate conditions, the difference of the N_2 adsorption amount among the adsorption pressure conditions was not severely reflected in the desorption time because of the reduced contact time and increased oxygen purge amount.

Comparison of Desorption Dynamics Among Three Different Beds

Figure 10 shows the dimensionless desorption curves in three different adsorption beds under the same conditions. Like the dimensionless breakthrough curves in Fig. 5, the dimensionless time at each bed was calculated by the interstitial velocity. As shown in this figure, the desorption of N_2 by oxygen purge was easily completed in the zeolite 10X bed. However, the desorption curve in the zeolite 13X bed showed the longest tail at all the beds. The desorption curve in the zeolite 5A bed showed intermediate behavior between the zeolite 10X and 13X beds. These phenomena can be explained easily with the shape of MTZ in the bed and temperature variation.

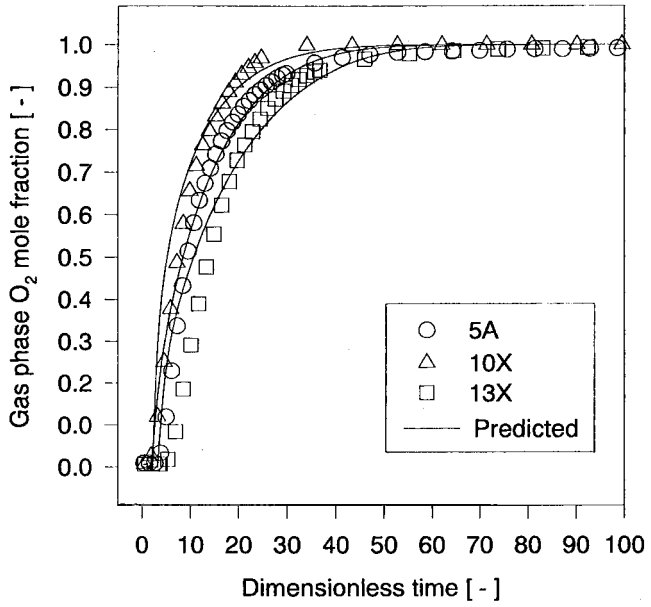

Figure 10. Comparisons of desorption curves among three different beds at 3 atm and 4 LSTP/min.

The N_2 concentration wave fronts in three different adsorption beds are shown in Fig. 11(a)–(c). As mentioned above, the N_2 MTZ in the zeolite 10X bed propagated fast to the product end by O_2 purge in Fig. 11(b), while those in the zeolite 5A and 13X beds showed slow movement in Fig. 11(a) and (c). Also, the N_2 MTZ in the early period of desorption showed favorable shape in all the beds. However, the N_2 MTZ in all the beds changed from nearly linear shape to the slightly unfavorable shape after sufficient time had passed because of the increased partial pressure of O_2. Especially, the unfavorable shape of desorption was more prominent in the zeolite 10X bed than in the other two beds because the adsorption isotherm of N_2 on zeolite 10X in Fig. 2 was more favorable than the others.

Figure 12 shows the dimensionless desorption temperature variation in the three different beds. In all cases, temperature decreased rapidly because of the heat of desorption by N_2 in the bed. However, after temperature excursion had reached a minimum, heat exchange between bed and surroundings and the purge gas temperature caused temperature increase toward the entrance temperature. However, after desorption, the temperature did not reach to purge gas temperature because of the slow heat transfer rate between the bed and surroundings, as well as the heat capacities of adsorbent and wall.

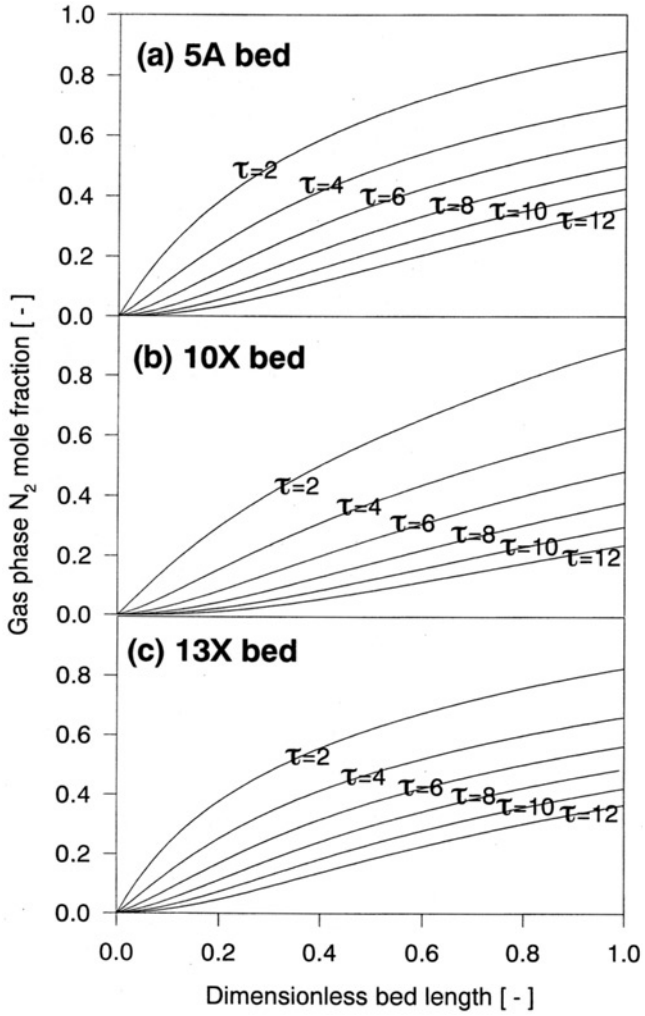

Figure 11. N_2 concentration profiles along the zeolite (a) 5A, (b) 10X, and (c) 13X beds under the desorption experiments at 3 atm and 4 LSTP/min.

The temperature decrease was most severe in the zeolite 13X bed and least in the zeolite 10X bed, which was opposite from the adsorption results in Fig. 6. This was because, in the desorption experiment, more amount of N_2 in the zeolite 13X bed was adsorbed than that in other two beds. However, the temperature profile in the zeolite 5A bed quickly approached at the purge gas temperature

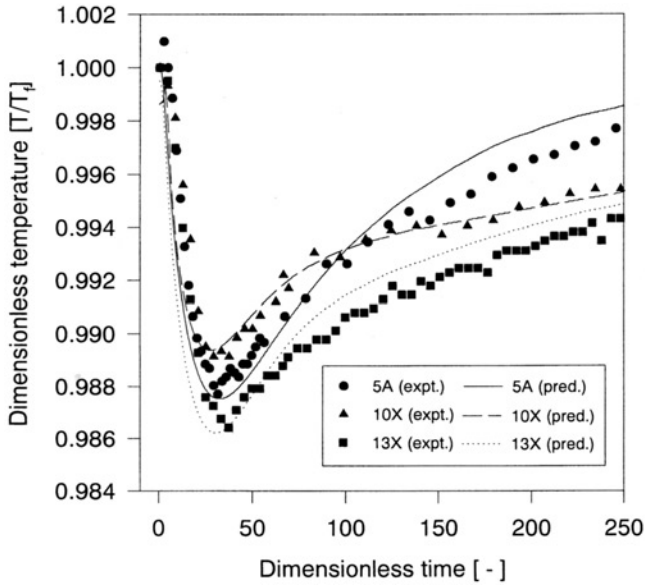

Figure 12. Experimental and predicted temperature curves of desorption experiments in the middle of three different beds at 3 atm and 4 LSTP/min.

compared with the zeolite 10X and 13X beds, which was similar to the result of the adsorption.

Figure 13 shows the heat effect on the desorption curves in the isothermal, adiabatic, and nonisothermal/nonadiabatic conditions. In contrast to the results of the adsorption study, the desorption temperature variations did not have any meaningful effect on the desorption behavior because the desorption of N_2 was mainly conducted by the increase of partial pressure of O_2 in the bed.

CONCLUSIONS

The adsorption and desorption dynamics of air were studied theoretically and experimentally in the zeolite 5A, 10X, and 13X beds. The breakthrough and desorption characteristics of all the beds were compared with respect to the breakthrough and desorption times, tailing effect, and temperature variation with the effects of pressure and flow rate.

The low feed flow rate and high adsorption pressure caused the prolongation of breakthrough time. However, in high feed flow rate, the effects

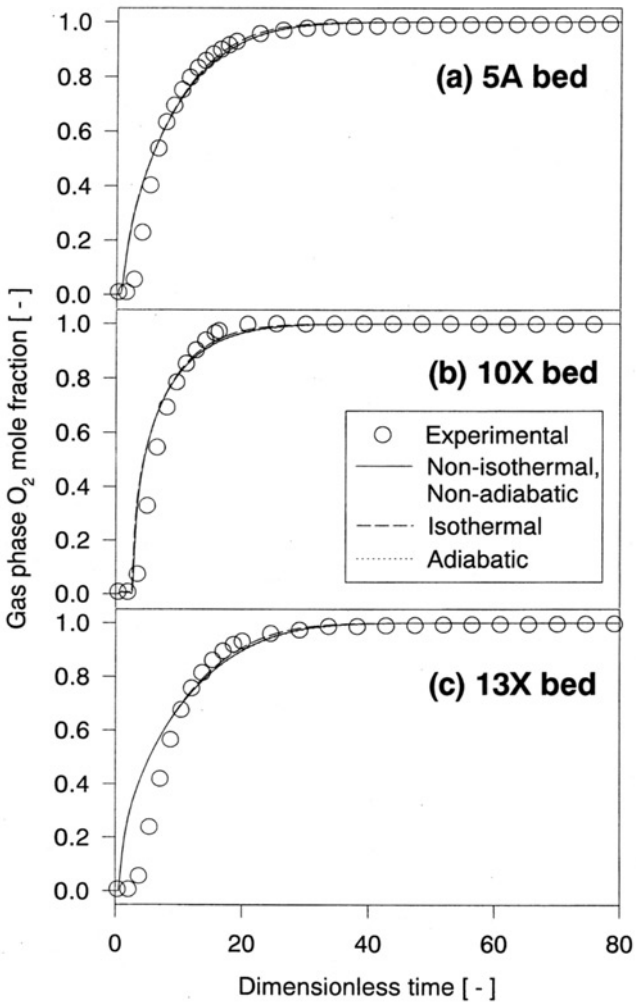

Figure 13. Comparisons of experimental and predicted desorption curves of the zeolite (a) 5A, (b) 10X, and (c) 13X beds on the three different temperature conditions at 3 atm and 4 LSTP/min.

of adsorption pressure on the breakthrough time were weakened with an increase in the feed flow rate. In addition, the effects of feed flow rate on the breakthrough time were decreased with high adsorption pressure. As a result, the feed and purge rates were more important factors for deciding the breakthrough and

desorption times than the adsorption and desorption pressures in the experimental range. In the case of the heats of adsorption and desorption, the thermal effect in the adsorption step was small but not negligible while this effect could be neglected in the desorption step.

The breakthrough curves in the zeolite 5A and 13X beds were similar in shape, while the breakthrough time was slightly longer in the zeolite 5A bed than in the zeolite 13X bed. In addition, the breakthrough curve in the zeolite 13X bed showed the longest tail. The MTZs in the zeolite 5A and 13X beds were not sharp compared with that in the zeolite 10X bed due to the less favorable N_2 isotherms of those adsorbents. The breakthrough curves in the zeolite 10X bed showed the shortest breakthrough time, but the sharpest MTZ with the isothermal behavior.

Through the desorption experiments at high pressure conditions, the desorption characteristics of all the beds were compared. In the high pressure purge applied for the bed adsorbed in the high adsorption pressure condition, the desorption time became longer at the bed adsorbed at the low adsorption pressure condition. Moreover, the effect of the purge flow rate increased with an increase in the purge pressure. Comparing the zeolite 5A bed with the zeolite 13X bed, desorption was more easily completed in the zeolite 13X bed than in the zeolite 5A bed. The desorption time was the shortest in the zeolite 10X bed because of the comparatively small adsorption amount. In addition, the shape of desorption curve in the zeolite 10X bed was the sharpest, similar to the result of the breakthrough curve.

NOMENCLATURE

A_W	cross sectional area of the wall (cm^2)
B	equilibrium parameter for LRC model (atm^{-1})
$\hat{B}$	dimensionless equilibrium parameter for LRC model (–)
c_i	i component concentration in bulk phase (mol/cm^3)
C_{pg}, C_{ps}, C_{pw}	gas, pellet, and wall heat capacity, respectively (cal/g K)
D_e	effective diffusivity defined by solid diffusion model (cm^2/sec)
D_L	axial dispersion coefficient (cm^2/sec)
$-\Delta H$	average heat of adsorption (cal/mol)
k	parameter for LRC model
K	proportionality parameter for LDF model (–)
K_L	axial thermal conductivity (cal/cm sec K)
L	bed length (cm)
p	total pressure (atm)
P	dimensionless total pressure (–)
Pe	Peclet number of mass transfer (–)

Pe_T	Peclet number of heat transfer (–)
q	adsorbed phase concentration
q_m	equilibrium parameter for LRC model (mol/g)
Q	dimensionless adsorbed phase concentration (–)
R	gas constant (cal/mol K)
R_p	radius of pellet (cm)
R_{Bi}, R_{Bo}	inside and outside radius of the bed, respectively (cm)
t	time (sec)
T	temperature (K)
T_f	temperature of feed (K)
T_{atm}	temperature of atmosphere (K)
u	interstitial velocity (cm/sec)
U	dimensionless interstitial velocity (–)
x	dimensionless axial distance (–)
y_i	mole fraction of species i
z	axial distance in bed from the inlet (cm)

Greek Letters

ε,ε_t	voidage of adsorbent bed and total void fraction, respectively (–)
ρ_g, ρ_p, ρ_B, ρ_w	gas density, pellet density, bulk density and bed wall density, respectively (g/cm^3)
τ	dimensionless time (–)
Θ	dimensionless temperature (–)
y_i	mole fraction of i component (–)
ω	LDF coefficient (sec^{-1})
$\hat{\omega}$	dimensionless LDF coefficient (–)

Superscripts

*	equilibrium value
–	average value
∧	dimensionless value

Subscripts

w	wall value
0	reference value

ACKNOWLEDGMENT

This work was supported by Korea Research Foundation Grant (KRF-2001-005-E0003).

REFERENCES

1. Yang, R.T. *Gas Separation by Adsorption Processes*; Butterworths: Boston, 1987.
2. Hayashi, S.; Kawai, M.; Kaneko, T. Dynamics of High Purity Oxygen PSA. Gas. Sep. Purif. **1996**, *10* (1), 19–23.
3. Rege, S.U.; Yang, R.T. Kinetic Separation of Oxygen and Argon Using Molecular Sieve Carbon. Adsorption **2000**, *6*, 15–22.
4. Sircar, S.; Hanley, B.F. Production of Oxygen Enriched Air by Rapid Pressure Swing Adsorption. Adsorption **1995**, *1*, 313–320.
5. Budner, Z.; Dula, J.; Podstawa, W.; Gawdzik, A. Study and Modeling of the Vacuum Swing Adsorption(VSA) Process Employed in the Production of Oxygen. Trans. IchemE **1999**, *77* (A), 405–412.
6. Kumar, R. Vacuum Swing Adsorption Process for Oxygen Production—A Historical Perspective. Sep. Sci. Technol. **1996**, *31* (7), 877–893.
7. Ruthven, D.M. *Pressure Swing Adsorption*; VCH: New York, 1994.
8. Malek, A.; Farooq, S. Effect of Velocity Variation on Equilibrium Calculations from Multi-Component Breakthrough Experiments. Chem. Eng. Sci. **1997**, *52* (3), 443–447.
9. Sircar, S.; Kumar, R. Effects of Column Nonisothermality or Nonadiabaticity on the Adsorption Breakthrough Curves. Ind. Eng. Chem. Res. **1983**, *22*, 10–15.
10. Xiu, G. Modeling Breakthrough Curves in a Fixed Bed of Activated Carbon Fiber—Exact Solution and Parabolic Approximation. Chem. Eng. Sci. **1996**, *51* (16), 4039–4041.
11. Yang, J.; Han, S.; Cho, C.; Lee, C.-H.; Lee, H. Bulk Separation of Hydrogen Mixtures by a One-column PSA Process. Sep. Technol. **1995**, *5*, 239–249.
12. Kvamsdal, H.K.; Hertzberg, T. A Preliminary Design Study of a Multicomponent PSA Gas Separation System. Chem. Eng. Sci. **1996**, *35*, 213–224.
13. Saitou, T.; Sugiyama, K. Hydrogen Purification with Metal Hydride Sintered Pellets Using Pressure Swing Adsorption Method. J. Alloys Comp. **1995**, *231*, 865–870.
14. Kikkinides, E.S.; Yang, R.T. Effects of Bed Pressure Drop on Isothermal and Adiabatic Adsorber Dynamics. Chem. Eng. Sci. **1993**, *48*, 1545–1554.
15. Rota, R.; Wanket, P.C. Intensification of Pressure Swing Adsorption Processes. AIChE J. **1990**, *36* (9), 1299–1312.
16. Ahn, H.; Lee, C.-H.; Seo, B.; Yang, J.; Baek, K. Backfill Cycle of a Layered Bed H_2 PSA Process. Adsorption **1999**, *5*, 419–433.

17. Yang, J.; Seo, B.K.; Baek, K.H.; Ko, S.-M.; Lee, C.H. Effects of Pressure Drop on Non-isothermal PSA Process. Korean J. Chem. Eng. **1998**, *15* (2), 211–216.
18. Jee, J.-G.; Kim, M.-B.; Lee, C.-H. Adsorption Dynamics of H_2 Mixtures in Layered Bed: Binary, Ternary, and Five-Component Mixture. Ind. Eng. Chem. Res. **2001**, *40* (3), 868–878.
19. Ahn, H.; Chun, C.; Park, M.; Ahn, I.-K.; Lee, C.-H. Thermal Effects on the Breakthrough Curve of a Hydrogen Ternary System at a Fixed Bed. Sep. Sci. Technol. **2001**, *36* (10), 2117–2141.
20. Hassan, M.M.; Raghavan, N.S.; Ruthven, D.M. Numerical Simulation of a Pressure Swing Air Separation System—A Comparative Study of Finite Difference and Collocation Methods. Can. J. Chem. Eng. **1987**, *65*, 512–516.
21. Yang, J.; Lee, C.-H. Adsorption Dynamics of a Layered Bed PSA for H_2 Recovery from Coke Oven Gas. AIChE J. **1998**, *44* (6), 1325–1334.
22. Sircar, S.; Hufton, J.R. Why Does the Linear Driving Force Model for Adsorption Kinetics Work? Adsorption **2000**, *6*, 137–147.
23. Suzuki, M. *Adsorption Engineering*; Kodansha Ltd.: Tokyo, 1990.
24. Sorial, G.A.; Granville, W.H.; Daly, W.O. Adsorption Equilibria for Oxygen and Nitrogen Gas Mixtures on 5A Molecular Sieves. Chem. Eng. Sci. **1983**, *38* (9), 1517–1523.
25. Sircar, S.; Hanley, B.F. Fractionated Vacuum Swing Adsorption for Air Separation. Sep. Sci. Technol. **1993**, *28* (17&18), 2553–2565.
26. Chou, C.-T.; Ju, D.-M.; Chang, S.-C. Simulation of a Fractionated Vacuum Swing Adsorption Process for Air Separation. Sep. Sci. Technol. **1998**, *33* (13), 2059–2073.
27. Rege, S.U.; Yang, R.T. Limits for Air Separation Adsorption with LiX Zeolite. Ind. Eng. Chem. Res. **1997**, *36*, 5358–5365.
28. Ahn, H.; Lee, C.-H. Sorption Kinetics of N_2, Co and CH_4 on Pelletized Zeolite 4A, 5A and 10X. J. Chem. Eng. Jpn **2002**, *35* (4), 334–345.
29. Farooq, S.; Ruthven, D.M.; Boniface, H.A. Numerical Simulation of a Pressure Swing Adsorption Oxygen Unit. Chem. Eng. Sci. **1989**, *44* (12), 2809–2816.
30. Waldron, W.E.; Sircar, S. Parametric Study of a Pressure Swing Adsorption Process. Adsorption **2000**, *6*, 179–188.

Received October 2001
Revised March 2002